Chapter 2.12. Inelastic Scattering of Electrons in Solids

S. Tanuma[a] and C. J. Powell[b]

[a]National Institute for Materials Science, 1-2-1 Sengen, Tsukuba, Ibaraki 305-0047, Japan (tanuma.shigeo@nims.go.jp)

[b]Materials Measurement Science Division, National Institute of Standards and Technology, Gaithersburg, Maryland 20899-8370, USA (cedric.powell@nist.gov)

Abstract

An overview is given of inelastic electron scattering in solids with an emphasis on calculations and measurements of electron inelastic mean free paths (IMFPs). There is generally good agreement between IMFPs calculated from optical data and IMFPs measured by elastic-peak electron spectroscopy for electron energies greater than 100 eV. For lower energies, however, there are significant differences between these calculated IMFPs and IMFPs determined from X-ray absorption fine structure experiments.

Keywords

Electron; inelastic mean free path; inelastic scattering.

2.12.1. Introduction

Information on the inelastic scattering of electrons in solids is important in theories of X-ray absorption fine structure (Rehr & Albers, 2000) and to various applications ranging from radiation physics and radiation transport to thin-film analysis in the transmission electron microscope (TEM) and surface analysis by Auger-electron spectroscopy and X-ray photoelectron spectroscopy. A key parameter in these applications is the electron inelastic mean free path (IMFP), λ, which is simply related to the total cross section for inelastic scattering, σ, and the number density of atoms per unit volume in the solid, N:

$$\lambda = 1/(\sigma N) . \qquad (2.12.1)$$

We will give a brief summary of efforts to calculate and measure IMFPs after first giving some historical information that will guide the later discussion.

2.12.2. Historical background

In the mid-1950s, a number of groups were measuring the energy-loss spectra of 20 keV to 50 keV electrons transmitted through thin sample films (e.g., of 50 nm thickness) of various solids (Marton, 1956; Pines, 1956). At that time, three main theories had been proposed to describe the observed energy losses. First, Leder *et al*. (1956) found numerical correlations between energy losses measured for many solids and the positions of fine structure in near-edge X-ray absorption spectra. These correlations suggested that the energy losses were due predominantly to single-electron excitations that could be related to the band structure of each solid. Second, Pines (1956) and coworkers proposed that the energy losses were due to plasma oscillations of the valence electrons, i.e., to bulk plasmons. While good correlations were found between observed and predicted energy losses for some solids (e.g., the so-called free-electron solids such as Mg, Al, and Si), there were appreciable inconsistencies for other solids (e.g., transition and noble metals). Third, a dielectric model for describing inelastic scattering had been proposed by Fano (1956), but the lack of reliable optical data for the region of interest (wavelengths between 50 nm and 400 nm) made interpretations difficult.

Subsequent work has shown that the dielectric model, as described by Fano (1956) and many others, provided a comprehensive description of the inelastic scattering of electrons in solids. It is now recognized that this model incorporates excitations of both bulk plasmons and single-electron excitations. The probability of inelastic scattering in the limit of zero momentum transfer is proportional to the energy-loss function (ELF), $\mathrm{Im}(-1/\varepsilon) = \varepsilon_2/(\varepsilon_1^2 + \varepsilon_2^2)$, where ε_1 and ε_2 are the real and imaginary parts of the complex dielectric constant, ε. ε_1 and ε_2 are simply related to the conventional optical constants, the index of refraction, n, and the extinction coefficient, k, by $\varepsilon_1 = n^2 - k^2$ and $\varepsilon_2 = 2nk$. For valence-electron excitations (typically involving energy losses less than about 100 eV), $\varepsilon_1^2 + \varepsilon_2^2$ is usually appreciably different from unity and there is a large difference between energy-loss and optical-absorption spectra. Maxima may also occur in the ELF at energy losses or optical frequencies near those where $\varepsilon_1 = 0$ and $\varepsilon_2 << 1$; these maxima can be identified as bulk plasmons. There may also be maxima in the ELF near frequencies for which there are maxima in ε_2; these maxima can be identified as single-electron excitations or interband transitions. Parametric calculations show how the positions and intensities of structure in the ELF can be related to the magnitude of ε_1 and to structure in ε_2 (Powell, 1969). For

inner-shell excitations (typically involving energy losses greater than about 100 eV), $\varepsilon_1 \approx 1$ and $\varepsilon_2 << 1$ so that $\mathrm{Im}(-1/\varepsilon) \approx \varepsilon_2$ and energy-loss spectra are similar to X-ray absorption spectra.

In an interesting application, Werner *et al*. (2009) have shown that optical properties of solids for photon energies between 0.5 eV and 70 eV can be derived from reflection energy-loss spectra acquired at two different primary energies. Measurements of inner-shell excitations in energy-loss spectroscopy of electrons transmitted through thin films, particularly in the TEM, have now become a useful method of thin-film analysis (Egerton, 2011).

2.12.3. Calculations of electron inelastic mean free paths

2.12.3.1. Algorithms

We describe several approaches that have been used to calculate IMFPs.

With use of the first Born approximation, the differential cross section (DCS) for inelastic scattering per atom or molecule for energy loss ω and momentum transfer q in condensed matter is given by (Schnatterly, 1979; Powell, 1984):

$$\frac{d^2\sigma}{d\omega dq} = \frac{1}{\pi NE}\mathrm{Im}\left[\frac{-1}{\varepsilon(\omega,q)}\right]\frac{1}{q} \quad , \tag{2.12.2}$$

where E is the electron energy and $\mathrm{Im}[-1/\varepsilon(\omega,q)]$ is the ELF which is now defined by the complex dielectric constant $\varepsilon(\omega, q)$. We have used Hartree atomic units in Eq. (2.12.2) in which $m_e = e = \hbar = 1$ where m_e is the electron rest mass, e is the elementary charge, and $\hbar$ is the reduced Planck constant.

The key material parameter in Eq. (2.12.2) is the ELF. If this is known, the IMFP at an electron energy E can be calculated from an integration of the DCS:

$$\frac{1}{\lambda} = \frac{1}{\pi E}\iint_D \frac{1}{q}\mathrm{Im}\left[\frac{-1}{\varepsilon(\omega,q)}\right]dqd\omega \tag{2.12.3}$$

The integration domain D is determined from the maximum and minimum energy losses and the largest and smallest kinematically-allowed momentum transfers for a given energy E and ω:

$$D = \left\{(\omega,q): 0 \le \omega \le E - E_{\mathrm{F}}, \sqrt{2}\left[\sqrt{E} - \sqrt{(E-\omega)}\right] \le q \le \sqrt{2}\left[\sqrt{E} + \sqrt{(E-\omega)}\right]\right\}, \tag{2.12.4}$$

where E_{F} is the Fermi energy of the material of interest.

Unfortunately, the ELF is not known for most materials. For a limited number of materials, optical data are available over a sufficiently large range of photon energies from which the optical ELF, $\mathrm{Im}\left[-1/\varepsilon(\omega,q=0)\right]$, can be determined. We then have to use an extension algorithm to determine the *q*-dependence of the ELF. We now briefly describe three of these algorithms.

Penn (1987) proposed an algorithm now known as the Full Penn Algorithm (FPA) for calculations of $\mathrm{Im}\left[-1/\varepsilon(q,\omega)\right]$ in Eq. (2.12.3). The FPA is based on the Lindhard model dielectric function and the use of measured optical ELF data for a given material. The ELF in Eq. (2.12.2) is then given by

$$\mathrm{Im}\left[\frac{-1}{\varepsilon(q,\omega)}\right]=\int_0^\infty g(\omega_p)\,\mathrm{Im}\left[\frac{-1}{\varepsilon^L(q,\omega;\omega_p)}\right]d\omega_p\,, \tag{2.12.5}$$

where ε^L denotes the Lindhard model dielectric function for a free-electron gas with plasmon energy $\omega_p\left(=\sqrt{4\pi n}\right)$, n is the electron density, and $g(\omega_p)$ is a coefficient introduced to satisfy the condition $\mathrm{Im}[-1/\varepsilon(q=0,\omega)]=\mathrm{Im}[-1/\varepsilon(\omega)]$. The coefficient $g(\omega_p)$ is

$$g(\omega)=\frac{2}{\pi\omega}\,\mathrm{Im}\left[\frac{-1}{\varepsilon(\omega)}\right]. \tag{2.12.6}$$

The ELF from the FPA in Eq. (2.12.5) can be described as the sum of two contributions, one associated with the plasmon pole and the other with single-electron excitations (Mao *et al*., 2008):

$$\mathrm{Im}\left[\frac{-1}{\varepsilon(q,\omega)}\right]=\mathrm{Im}\left[\frac{-1}{\varepsilon(q,\omega)}\right]_{pl}+\mathrm{Im}\left[\frac{-1}{\varepsilon(q,\omega)}\right]_{se}. \tag{2.12.7}$$

Details of the calculation procedures for each term in Eq. (2.12.7) have been published by Shinotsuka *et al*. (2015). This algorithm has been used to calculate IMFPs for energies from 50 eV to 200 keV.

A second algorithm for IMFP calculations was proposed by Abril *et al*. (1998). They recommended use of the Mermin (1970) dielectric function, $\varepsilon_M(q,\omega)$, since this approach (unlike the Lindhard dielectric function used in the FPA) takes the

plasmon lifetime into account.

The ELF in Eq. (2.12.3) is separated into two components, one for valence-electron excitations and the other for inner-shell excitations:

$$\mathrm{Im}\left[\frac{-1}{\varepsilon(q,\omega)}\right] = \mathrm{Im}\left[\frac{-1}{\varepsilon(q,\omega)}\right]_{VB} + \mathrm{Im}\left[\frac{-1}{\varepsilon(q,\omega)}\right]_{IS}. \quad (2.12.8)$$

The former component is fitted with a selected number, L, of Drude functions,

$$\mathrm{Im}\left[\frac{-1}{\varepsilon(q,\omega)}\right]_{VB} \approx \sum_{i=1}^{L} A_i \,\mathrm{Im}\left\{\frac{-1}{\varepsilon_M\left(q,\omega;\omega_{pi},\gamma_i\right)}\right\}, \quad (2.12.9)$$

where A_i, ω_{pi}, and γ_i are fitting parameters that represent the oscillator strength, peak energy, and width of the i-th oscillator, respectively, so that

$$\mathrm{Im}\left\{\frac{-1}{\varepsilon(\omega)}\right\} = \sum_{i=1}^{L} A_i \,\mathrm{Im}\left\{\frac{-1}{\varepsilon_M\left(q=0,\omega;\omega_{pi},\gamma_i\right)}\right\} \equiv \sum_{i=1}^{L} A_i \frac{\gamma_i \omega \omega_{pi}^2}{\left(\omega^2-\omega_{pi}^2\right)^2+\gamma_i^2\omega^2}. \quad (2.12.10)$$

That is, a satisfactory fit has to be made with Eq. (2.12.10) to a set of optical ELF data, typically from about 1 eV to the threshold energy for the lowest inner-shell excitation.

For inner-shell excitations, Heredia-Avalos *et al*. (2005) utilized atomic generalized oscillator strengths (GOSs) from hydrogenic calculations for the second term of Eq. (2.12.8):

$$\mathrm{Im}\left[\frac{-1}{\varepsilon(q,\omega)}\right]_{IS} = \frac{2\pi^2 N}{\omega}\sum_j \alpha_j \sum_{nl} \frac{df_{nl}^{(j)}(q,\omega)}{d\omega}, \quad (2.12.11)$$

where $df_{nl}^{(j)}(q,\omega)/d\omega$ is the GOS for the *(n, l)* subshell of the *j*-th element.

A third algorithm was proposed by Da *et al*. (2014). They developed what they called an extended Mermin (EM) method to avoid separate IMFP calculations for valence-band and inner-shell electrons. The EM method employs an unlimited number of Mermin oscillators and allows negative oscillators (i.e., negative values of A_i in Eqs. (2.12.9) and (2.12.10)) to take into account not only a generally small number of valence-electron excitations for observed structure in the ELF, as is common with the usual Mermin algorithm, but also infrared transitions and inner-shell excitations that can display "edges" and continua.

We briefly mention several other IMFP calculations. IMFPs can be obtained from first-principles calculations of hot-electron lifetimes, typically for energies less

than 4 eV although some calculations were made for energies up to 100 eV (Chulkov *et al*., 2006). That is, there was no use of optical ELF data. Nagy and Echenique (2012) reported what they term lower bounds for Cu IMFPs at energies less than 75 eV based on Fermi liquid (FL) theory. Nguyen-Truong (2016) has calculated the Cu ELF using the adiabatic local-density approximation in the framework of time-dependent density-functional theory (DFT) for energy losses up to 60 eV. This ELF agreed well with an earlier DFT calculation by Werner *et al*. (2009). The ELF was then used to compute IMFPs for Cu at energies between 1 eV and 100 eV (Nguyen-Truong (2016)). Finally, de Vera and Garcia-Molina (2019) have reported IMFPs for water, Al, Cu, and Au based on higher-order corrections to the first Born approximation.

2.12.3.2. ELF data

The first three algorithms described above require optical data, typically for photon energies between about 1 eV and an upper limit that can be as high as 200 keV (Shinotsuka *et al*., 2015), from which the optical ELF (i.e., for $q = 0$) can be calculated. The needed data come from a variety of sources, as described by Tanuma *et al*. (2011) and Shinotsuka *et al*. (2015). It is important to check the reliability or internal consistency of optical ELFs using two useful sum rules (Tanuma *et al*., 1993, 2011).

ELFs for valence-electron excitations have also been derived from density functional theory by Werner *et al*. (2009) and by Chantler & Bourke (2014).

2.12.3.3. *Calculated IMFPs for elemental solids and compounds*

Tanuma *et al*. (2011) reported IMFP calculations for 41 elemental solids (Li, Be, graphite, diamond, glassy C, Na, Mg, Al, Si, K, Sc, Ti, V, Cr, Fe, Co, Ni, Cu, Ge, Y, Nb, Mo, Ru, Rh, Pd, Ag, In, Sn, Cs, Gd, Tb, Dy, Hf, Ta, W, Re, Os, Ir, Pt, Au, and Bi) for electron energies between 50 eV and 30 keV using the FPA while Shinotsuka *et al*. (2015) reported similar calculations for the same solids for energies between 50 eV and 200 keV using a relativistic version of the FPA. Figure 2.12.1 shows a summary plot of the IMFPs calculated by Shinotsuka *et al*. for the 41 elemental solids as a function of electron energy between 10 eV to 10 keV. While the FPA is expected to give reliable results for energies above 50 eV (Tanuma *et al*., 1991), we show IMFPs at lower energies in Fig. 2.12.1 to indicate trends.

Figure 2.12.2 shows IMFPs for 42 inorganic compounds (AgBr, AgCl, AgI, Al_2O_3, AlAs, AlN, AlSb, cubic BN, hexagonal BN, CdS, CdSe, CdTe, GaAs, GaN, GaP, GaSb, GaSe, InAs, InP, InSb, KBr, KCl, MgF_2, MgO, NaCl, $NbC_{0.712}$, $NbC_{0.844}$, $NbC_{0.93}$,

PbS, PbSe, PbTe, SiC, SiO_2, SnTe, $TiC_{0.7}$, $TiC_{0.95}$, $VC_{0.76}$, $VC_{0.86}$, $Y_3Al_5O_{12}$, ZnS, ZnSe, and ZnTe) that were calculated by Shinotsuka *et al.* (2019) using the relativistic FPA, again for energies between 10 eV and 10 keV. We note that ELFs for many of these compounds were calculated from the WIEN2k and FEFF codes.

For energies between 1 keV and 10 keV, there is at least a factor of five difference between the smallest and largest IMFPs (at a given energy) for the elemental solids in Fig. 2.12.1 and a factor of 2.2 for the inorganic compounds in Fig. 2.12.2. These variations in IMFP magnitudes are due mainly to variations in bulk densities. Minima in the IMFP plots occur at energies between about 10 eV and about 100 eV. These variations are associated with differences in the shapes of the ELFs for the solids.

2.12.3.4. Predictive IMFP formula

Tanuma *et al.* (1994) developed the following predictive IMFP formula from an analysis of calculated IMFPs for their original group of 27 elemental solids (Tanuma *et al*., 1991) and for a group of 14 organic compounds for energies between 50 eV and 2 keV:

$$\lambda = \frac{E}{E_p^2[\beta \ln(\gamma E) - (C/E) + (D/E^2)]}, \text{ (nm)} \qquad (2.12.12a)$$

where E is the electron energy (in eV), $E_p = 28.82(N_v\rho/M)^{1/2}$ (eV) is the bulk plasmon energy (in eV), N_v is the number of valence electrons per atom or molecule, ρ is the bulk density (in g/cm^3), and M is the atomic or molecular weight. Simple expressions were found for the four parameters in Eq. (2.12.11a) in terms of material properties:

$$\beta = -1.0 + 9.44/\left(E_p^2 + E_g^2\right)^{0.5} + 0.69\rho^{0.1}, \text{ (eV}^{-1}\text{ nm}^{-1}\text{)} \qquad (2.12.12b)$$

$$\gamma = 0.191\rho^{-0.5}, \text{ (eV}^{-1}\text{)} \qquad (2.12.12c)$$

$$C = 19.7 - 9.1U, \text{ (nm}^{-1}\text{)} \qquad (2.12.12d)$$

$$D = 534 - 208U, \text{ (eV nm}^{-1}\text{)} \qquad (2.12.12e)$$

where E_g is the bandgap energy (in eV) for nonconductors, and $U = N_v\rho/M$. Equation (2.12.12) is the TPP-2M formula of Tanuma *et al*. (1994) that can be used for estimating IMFPs in other materials. In later work, Tanuma *et al*. (2011) found that the TPP-2M formula was useful for energies up to 30 keV while Shinotsuka *et al*. (2015) developed a relativistic version that was useful for energies up to 200 keV. In the

former evaluation, the average root-mean-square (RMS) deviation between the calculated IMFPs for 41 elemental solids and the values from Eq. (2.12.12) was 12.3 %. Relatively large RMS deviations (up to 72 %) were found for diamond, graphite, and cesium, as found by Tanuma *et al*. (2005a). If these three elements were excluded in the comparisons, the average RMS deviation was 9.2 %.

2.12.4. Measurements of electron inelastic mean free paths

We briefly describe four experimental approaches that have been used to obtain IMFPs. All of these approaches rely on models of the relevant physical processes and auxiliary data.

2.12.4.1. Elastic-peak electron spectroscopy

IMFPs can be obtained from measurements of ratios of elastically backscattered electron yields from a sample of interest and a reference material for which the IMFP is known, a technique known as elastic-peak electron spectroscopy (EPES) (Powell & Jablonski 1999, 2009). These ratios, determined for a range of incident electron energies, are then compared with corresponding ratios from Monte Carlo simulations in which the sample IMFP is a parameter. Ni, Cu, Ag, or Au are often chosen as reference materials since these materials showed good consistencies in comparisons of IMFPs calculated from optical data and IMFPs determined from EPES experiments (Powell & Jablonski, 1999).

2.12.4.2. Reflection electron energy-loss spectroscopy

Werner *et al*. (2009) analyzed reflection electron energy-loss spectra (REELS) for 17 elemental solids and derived their optical constants for photon energies between 0.5 eV and 70.5 eV. With these results and atomic photoabsorption data for higher photon energies, Werner *et al*. computed ELFs and then IMFPs using the Penn algorithm for energies between 100 eV and 10 keV. The average RMS deviation between these REELS IMFPs and the optical IMFPs of Tanuma *et al*. was 5.8 %. Werner *et al*. also commented that their REELS IMFPs were "indistinguishably similar" to those obtained from optical constants calculated using density functional theory.

2.12.4.3. X-ray absorption fine structure

Bourke and Chantler (2010) and Chantler and Bourke (2010) reported IMFPs of 5 eV to 120 eV electrons in Cu and Mo that were derived from high-accuracy measurements of X-ray absorption fine structure (XAFS). Measured spectra were

compared with corresponding calculated spectra (that included the effects of core-hole widths and thermal vibrations) and the IMFPs were obtained as measures of the additional broadening needed for the calculated spectra to agree with the measured spectra.

2.12.4.4. Photoelectron spectroscopy

Knapp *et al*. (1979) determined photoelectron lifetimes from an analysis of photoelectron spectra (PES) from a Cu(100) surface for energies between about 11 eV and 14 eV. These lifetimes were converted to IMFPs using a group velocity for the excited electrons based on a free-electron model.

Wertheim *et al*. (1992) measured PES of Li, Na, K, and Rb for photon energies between 22 eV and 140 eV. These spectra showed separate peaks due to photoemission from the surface layer of atoms in each metal as well as other peaks arising from other atoms, i.e., the bulk of the solid. The samples were prepared by vacuum evaporation onto a Ni(100) substrate cooled to 78 K, and the films had a (110) surface orientation. With use of model descriptions of surface and bulk lineshapes, they determined the fractional intensity of bulk emission, f_B, for each spectrum and equated this fraction to $\exp(-d/\lambda)$ where d is the (110) layer spacing. Wertheim *et al*. could thus determine IMFPs for each metal as a function of photoelectron energy. Pi *et al*. (2012) used the same method for determining IMFPs in GaAs for energies between about 24 eV and about 140 eV.

2.12.5. Comparisons of calculated IMFPs with experimental results

Two groups have reported IMFPs for elemental solids from EPES experiments, with Tanuma *et al*. (2005b) providing IMFPs for 13 elemental solids for energies between 50 eV and 5 keV and Werner *et al*. (2000, 2001) providing IMFPs for 24 elemental solids for energies between 50 eV and 3.4 keV. The average RMS difference between the optical IMFPs of Tanuma *et al*. (2011) and the EPES IMFPs of Tanuma *et al*. (2005b) was 12 % (for the 11 solids that were common to both data sets), while the average RMS difference between the optical IMFPs of Tanuma *et al*. (2011) and the EPES IMFPs of Werner *et al*. (2000, 2001) was 15 % (for the 17 solids that were common to both data sets).

We now show comparisons of calculated and measured IMFPs for an elemental solid, Cu, and an inorganic compound, GaAs. Figure 2.12.3 shows plots of

Cu IMFPs calculated from the FPA and EM methods by Shinotsuka *et al*. (2015), IMFPs from the FL calculations of Nagy and Echenique (2012), IMFPs from the DFT calculations of Nguyen-Truong (2016), IMFPs from the dielectric formalism including high-order corrections to the first Born approximation of de Vera & Garcia-Molina (2019), and IMFPs from the TPP-2M predictive formula (Eq. (2.12.11)) as a function of electron energy together with IMFPs determined from XAFS experiments (Bourke & Chantler, 2010), PES experiments (Knapp *et al*. (1979)), and EPES experiments (Tanuma *et al*., 2005b). The Cu IMFPs from the EM method in Fig. 2.12.3 agree well with those previously obtained with the Mermin method by Bourke and Chantler (2012).

For energies over 300 eV, we see good agreement among the Cu IMFPs calculated from the FPA, EM methods, and the dielectric formalism including the high-order corrections (HOC), and the TPP-2M formula with IMFPs from EPES experiments. For energies between 50 eV and 300 eV, IMFPs calculated from the EM method and from the TPP-2M formula generally agree well with IMFPs measured by the EPES and XAFS methods although the FPA results are larger than the measured values. For energies between 50 eV and 300 eV, IMFPs calculated from the HOC are in excellent agreement with IMFPs measured by the EPES and slightly larger than IMFPs measured by the XAFS method, from EM methods and from the TPP-2M formula. IMFPs from the DFT calculations of Nguyen-Truong (2016) are consistent with IMFPs from the EM method, IMFPs from the TPP-2M equation, and IMFPs from the XAFS experiments at about 100 eV but are smaller than those from the FPA. For energies less than 20 eV, however, the DFT IMFPs become consistent with the FPA IMFPs, IMFPs calculated from the HOC method, and the IMFPs measured by PES but are much larger than the XAFS IMFPs. The XAFS IMFPs are also appreciably smaller than the IMFPs calculated from the FPA and EM methods for energies less than 50 eV. These systematic differences at low energies could be due to correlation and exchange effects that were not included in the IMFP calculations from the FPA (Powell & Jablonski, 1999) and/or to surface excitations (Powell & Jablonski, 2009) although correlation and exchange effects are included in the DFT calculations. The IMFPs calculated by Nagy and Echenique (2012) for energies between 10 eV and 75 eV are described as “lower bounds”. These IMFPs are numerically similar to the IMFPs from EXAFS experiments for energies between 10 eV and about 50 eV but show a very different energy

dependence.

We point out that Rundgren (1999) found good agreement between measured current-voltage plots in a low-energy electron diffraction experiment with a Cu(111) surface and with calculated plots based on the FPA IMFPs of Tanuma *et al*. (1991) for energies between 30 eV and 190 eV. If the IMFPs in Cu were appreciably smaller than the FPA values (as indicated by the XAFS IMFPs in Fig. 2.12.3 for energies less than 100 eV), the calculated current-voltage plots would have had much larger peak widths.

Figure 2.12.4 shows comparisons of IMFPs for GaAs calculated from the FPA, IMFPs from the TPP-2M equation, IMFPs from EPES experiments (Krawczyk *et al*., 1988), and IMFPs derived from an analysis of PES experiments (Pi *et al*., (2012). We see generally good agreement among the calculated and measured IMFPs for energies from 20 eV to 5 keV. While there is some scatter in the IMFPs from the photoemission experiments, there is no indication of the substantial systematic differences between IMFPs from the FPA and IMFPs from XAFS experiments that were seen for Cu in Fig. 2.12.3.

2.12.6. Conclusions

Powell and Jablonski (2009) concluded that IMFPs calculated from optical data with the FPA have uncertainties of up to about 10 %. Their analysis was made for electron energies between 50 eV and about 5 keV. It is now apparent that similar calculations with the Mermin (1970) dielectric function or the extended Mermin method (Da *et al*., 2014) would be more reliable for energies less than about 100 eV. Significant disagreements exist between IMFPs determined from XAFS experiments and PES experiments, and between IMFPs from XAFS experiments and calculated IMFPs, particularly for energies less than about 100 eV, as indicated by the results for Cu in Fig. 2.12.3. Additional experiments or analyses are therefore needed to resolve these differences.

A database is available that provides IMFPs calculated from optical data, IMFPs from EPES experiments, and IMFPs from the TPP-2M predictive formula for electron energies from 50 eV to 10 keV (Powell & Jablonski, 2010).

References

Abril, I., Garcia-Molina, R., Denton, C. D., Perez-Peres, J., & Arista, R. (1998).

Dielectric description of wakes and stopping powers in solids. Phys. Rev. A 58, 357-366.

Bourke, J. D. & Chantler, C. T. (2010). Measurements of Electron Inelastic Mean Free Paths in Materials. Phys. Rev. Lett. 104, 206601.

Bourke, J. D. & Chantler, C. T. (2012). Electron Energy-Loss Spectra and Overestimation of Inelastic Mean Free Paths in Many-Pole Models. J. Phys. Chem. A 116, 3202-3205.

Chantler, C. T. & Bourke, J. D. (2010). X-ray Spectroscopic Measurement of Photoelectron Inelastic Mean Free Paths in Molybdenum. J. Phys. Chem. Letters 1, 2422-2427.

Chantler, C. T. & Bourke, J. D. (2014). Electron Inelastic Mean Free Path Theory and Density Functional Theory Resolving Discrepancies for Low-Energy Electrons in Copper. J. Phys. Chem. 118, 909-914.

Chulkov, E. V., Borisov, A. G., Gauyacq, J. P., Sanchez-Portal, D., Silkin, V. M., Zhukov, V. P., & Echenique, P. M. (2006). Electronic Excitations in Metals and at Metal Surfaces. Chem. Rev. 106, 4160-4206.

Da, B., Shinotsuka, H., Yoshikawa, H., Ding, Z. J., & Tanuma, S. (2014). Extended Mermin Method for Calculating the Electron Inelastic Mean Free Path. Phys. Rev. Letters 113, 063201.

Egerton, R. F. (2011). Electron Energy-loss Spectroscopy in the Electron Microscope, 3rd edition, Springer, New York.

Fano, U. (1956). Atomic Theory of Electromagnetic Interactions in Dense Materials. Phys. Rev. 103, 1202-1218.

Heredia-Avalos, S., Garcia-Molina, R., Fernández-Varea, J. M., & Abril, I. (2005). Calculated energy loss of swift He, Li, B, and N ions in SiO_2, Al_2O_3, and ZrO_2. Phys Rev. A 72, 052902.

Knapp, J. A., Himpsel, F. J., and Eastman, D. E. (1979). Experimental Energy Band Dispersions and Lifetimes for Valence and Conduction Bands of Copper Using Angle-Resolved Photoemission. Phys. Rev. B 19, 4952.

Krawczyk, M., Jablonski, A., Tougaard, S., Toth, J., Varga, D., & Gergely, G. (1988). The Inelastic Mean Free Path and the Inelastic Scattering Cross Section of Electrons in GaAs Determined from Highly Resolved Electron Energy Spectra. Surface Science 402–404, 491-495.

Leder, L. B., Mendlowitz, H., & L. Marton, L. (1956). Comparison of the Characteristic Energy Losses of Electrons with the Fine Structure of the X-ray Absorption Spectra. Phys. Rev. 101, 1460-1467.

Lindhard, J. (1954). On the Properties of a Gas of Charged Particles. K. Dan. Vidensk. Mat.-Fys. Medd. 28(8), 1-57.

Mao, S. F., Li, Y. G., Zeng, R. G., & Ding, Z. J. (2008). Electron Inelastic Scattering and Secondary Electron Emission Calculated without the Single Pole Approximation. J. Appl. Phys. 114907.

Marton, L. (1956). Experiments on Low-Energy Electron Scattering and Energy Losses. Rev. Mod. Phys. 28, 172-183.

Mermin, N. D. (1970). Lindhard Dielectric Function in the Relaxation-Time Approximation. Phys. Rev. B 1, 2362-2363.

Nagy, I., & Echenique, P. M. (2012). Mean Free Path of a Suddenly Created Fast Electron Moving in a Degenerate Electron Gas. Phys. Rev. B 85, 115131.

Nguyen-Truong, H. T. (2016). Low-Energy Electron Inelastic Mean Free Path in Materials. Appl. Phys. Letters 108, 172901.

Penn, D. R. (1987). Electron Mean-Free-Path Calculations Using a Model Dielectric Function. Phys. Rev. B 35, 482-286.

Pi, T.-W., Chen, B.-R., Huang, M.-L., Chiang, T.-H., Wertheim, G. K., Hong, M., & Kwo, J. (2012). Surface-Atom Core-Level Shift in GaAs(111)A-2x2. J. Phys. Soc. Jpn. 81, 064603.

Pines, D. (1956). Collective Energy Losses in Solids. Rev. Mod. Phys. 28, 184-198.

Powell, C. J. (1969). Analysis of Optical- and Inelastic-Electron-Scattering Data. Parametric Calculations. J. Opt. Soc. Am. 59, 738-743.

Powell, C. J. (1984). Inelastic Scattering of Electrons in Solids, in Electron Beam Interactions with Solids for Microscopy, Microanalysis, and Microlithography, edited by D. F. Kyser, D. E. Newbury, H. Niedrig, & R. Shimizu, 19-32. Chicago: Scanning Electron Microscopy.

Powell, C. J., Jablonski, A. (1999). Evaluation of Calculated and Measured Inelastic Mean Free Paths near Solid Surfaces. J. Phys. Chem. Ref. Data 28, 19-62.

Powell, C. J. & Jablonski, A. (2009). Surface Sensitivity of X-ray Photoelectron Spectroscopy. Nucl. Instr. Methods Phys. Res. A 601, 54-65.

Powell, C. J. & Jablonski, A. (2010). NIST Electron Inelastic-Mean-Free-Path Database. Version 1.2 (SRD 71), Standard Reference Data Program, National Institute of Standards and Technology, Gaithersburg, MD, 2010; http://www.nist.gov/srd/nist71.cfm.

Rehr, J. J. & Albers, R. C. (2000). Theoretical Approaches to X-ray Absorption Fine Structure, Rev. Mod. Phys. 72, 621-654.

Rundgren, J. (1999). Electron Inelastic Mean Free Path, Electron Attenuation Length, and Low-Energy Electron-Diffraction Theory. Phys. Rev. B 59, 5106-5114.

Schnatterly, S. E. (1979). Inelastic Electron Scattering Spectroscopy, in Solid State Physics edited by H. Ehrenreich, F. Seitz, & D. Turnbull, Vol. 34, 275-358. New York: Academic Press.

Shinotsuka, H., Tanuma, S., Powell, C. J., & Penn, D. R. (2015). Calculations of Electron Inelastic Mean Free Paths. IX. Data for 41 Elemental Solids over the 50 eV to 200 keV Range. Surf. Interface Anal. 47, 871-888; erratum: ibid. 47, 1132.

Shinotsuka, H., Tanuma, S., Powell, C. J., & Penn, D. R. (2019). Calculations of Electron Inelastic Mean Free Paths. XII. Data for 42 Inorganic Compounds over the 50 eV to 200 keV Range. Surf. Interface Anal. 51, 427-457.

Tanuma, S., Powell, C. J., & Penn, D. R. (1991). Calculations of Electron Inelastic Mean Free Paths. II. Data for 27 Elements over the 50 eV to 2000 eV Range. Surf. Interface Anal. 17, 911-926.

Tanuma, S., Powell, C. J., & Penn, D. R. (1993). Use of Sum Rules on the Energy-Loss Function for the Evaluation of Experimental Optical Data. J. Electron Spectrosc. Relat. Phenom. 62, 95-109.

Tanuma, S., Powell, C. J., & Penn, D. R. (1994). Calculations of Electron Inelastic Mean Free Paths. V. Data for 14 Organic Compounds over the 50 eV to 2000 eV Range. Surf. Interface Anal. 21, 165-176.

Tanuma, S., Powell, C. J., & Penn, D. R. (2005a). Calculations of Electron Inelastic Mean Free Paths. VIII. Data for 15 Elemental Solids over the 50 eV to 2000 eV Range. Surf. Interface Anal. 37, 1-14.

Tanuma, S., Shiratori, T., Kimura, T., Goto, K., Ichimura, S., & Powell, C. J. (2005b). Experimental Determination of Electron Inelastic mean Free Paths in 13 Elemental Solids in the 50 eV to 5000 eV Energy Range by Elastic-Peak Electron Spectroscopy. Surf. Interface Anal. 37, 833-845.

Tanuma, S., Powell, C. J., & Penn, D. R. (2011). Calculations of Electron Inelastic Mean Free Paths. IX. Data for 41 Elemental Solids over the 50 eV to 30 keV Range. Surf. Interface Anal. 43, 689-713.

Vera, de P., Garcia-Molina, R. (2019). Electron Inelastic Mean Free Paths in Condensed Matter Down to a Few Electronvolts. J. Phys. Chem. C 123, 2075-2083.

Werner, W. S. M., Tomastik, C., Cabela, T., Richter, G., & Störi, H. (2000). Electron Inelastic Mean Free Path Measured by Elastic Peak Electron Spectroscopy for 24 Solids between 50 and 3400 eV. Surf. Science 470, L123-L128.

Werner, W. S. M., Tomastik, C., Cabela, T., Richter, G., & Störi, H. (2001). Elastic Electron Reflection for Determination of the Inelastic Mean Free Path of Medium Energy Electrons in 24 Elemental Solids for Energies between 50 and 3400 eV. J. Electron Spectrosc. Relat. Phenom. 113, 127-135.

Werner, W. S. M., Glantschnig, K., & Ambrosch-Draxl, C. (2009). Optical Constants and Inelastic Electron-Scattering Data for 17 Elemental Metals. J. Phys. Chem. Ref. Data 38, 1013-1043.

Wertheim, G. K., Riffe, D. M., Smith, N. V., & Citrin, P. H. (1992). Electron Mean Free Paths in the Alkali Metals. Phys. Rev. B 46, 1955-1959.

Figure Captions

Fig. 2.12.1. Plots of IMFPs calculated by Shinotsuka *et al*. (2015) for 41 elemental solids (Li, Be, graphite, diamond, glassy C, Na, Mg, Al, Si, K, Sc, Ti, V, Cr, Fe, Co, Ni, Cu, Ge, Y, Nb, Mo, Ru, Rh, Pd, Ag, In, Sn, Cs, Gd, Tb, Dy, Hf, Ta, W, Re, Os, Ir, Pt, Au, and Bi) for electron energies between 10 eV and 10 keV.

Fig. 2.12.2. Plots of IMFPs calculated by Shinotsuka *et al*. (2019) for 42 inorganic compounds (AgBr, AgCl, AgI, Al_2O_3, AlAs, AlN, AlSb, cubic BN, hexagonal BN, CdS, CdSe, CdTe, GaAs, GaN, GaP, GaSb, GaSe, InAs, InP, InSb, KBr, KCl, MgF_2, MgO, NaCl, $NbC_{0.712}$, $NbC_{0.844}$, $NbC_{0.93}$, PbS, PbSe, PbTe, SiC, SiO_2, SnTe, $TiC_{0.7}$, $TiC_{0.95}$, $VC_{0.76}$, $VC_{0.86}$, $Y_3Al_5O_{12}$, ZnS, ZnSe, and ZnTe) for electron energies between 10 eV and 10 keV.

Fig. 2.12.3. Comparisons of Cu IMFPs calculated from the FPA (solid line) and EM (dot-dashed line) methods for electron energies between 10 eV and 10 keV, IMFPs from the FL calculations of Nagy & Echenique (2012) for energies between 10 eV and 75 eV (short-dashed line), IMFPs from the DFT calculations of Nguyen-Truong (2016) for energies between 10 eV and 100 eV (medium-dashed line), IMFPs from the dielectric formalism including high-order corrections (HOC) to the first Born approximation of Vera & Garcia-Molina (2019) for energies between 10 eV and 10 keV (dot and short-dashed line) and IMFPs from the TPP-2M predictive formula (long-dashed line) with Cu IMFPs determined from XAFS experiments (solid squares, Bourke & Chantler, 2010), PES experiments (solid triangles, Knapp *et al*. (1979)), and EPES experiments (solid circles, Tanuma *et al*., 2005b).

Fig. 2.12.4. Comparisons of GaAs IMFPs calculated from the FPA (solid line) by Shinotsuka *et al*. (2016) for electron energies between 10 eV and 10 keV and IMFPs from the TPP-2M predictive formula (dashed line) with IMFPs from EPES experiments (solid circles, Krawczyk *et al*., 1988) and IMFPs from PES experiments (solid triangles, Pi *et al*., 2012).

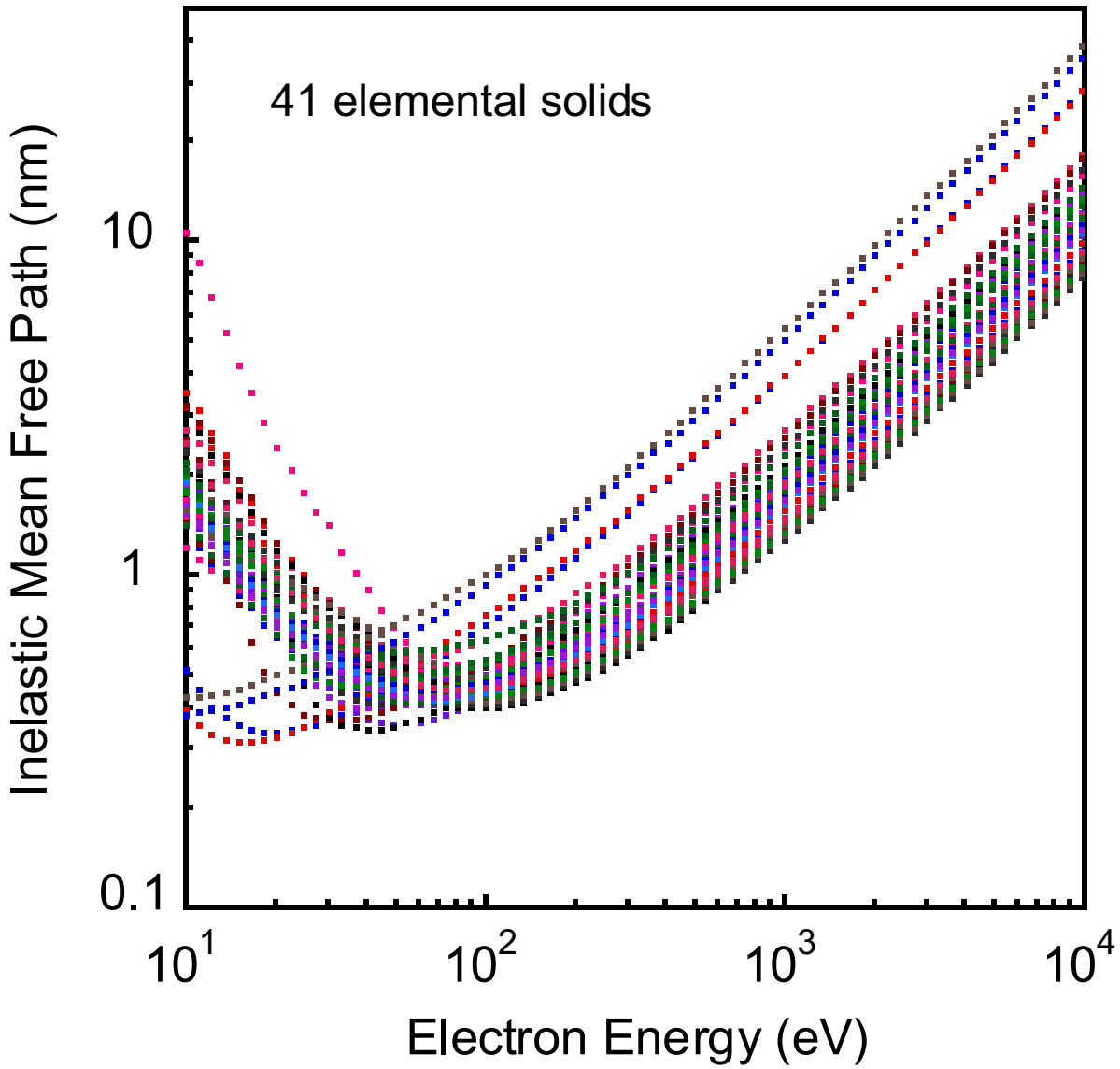
41 elemental solids
Inelastic Mean Free Path (nm)
10
1
0.1
10^1
10^2
10^3
10^4
Electron Energy (eV)

Fig. 2.12.1

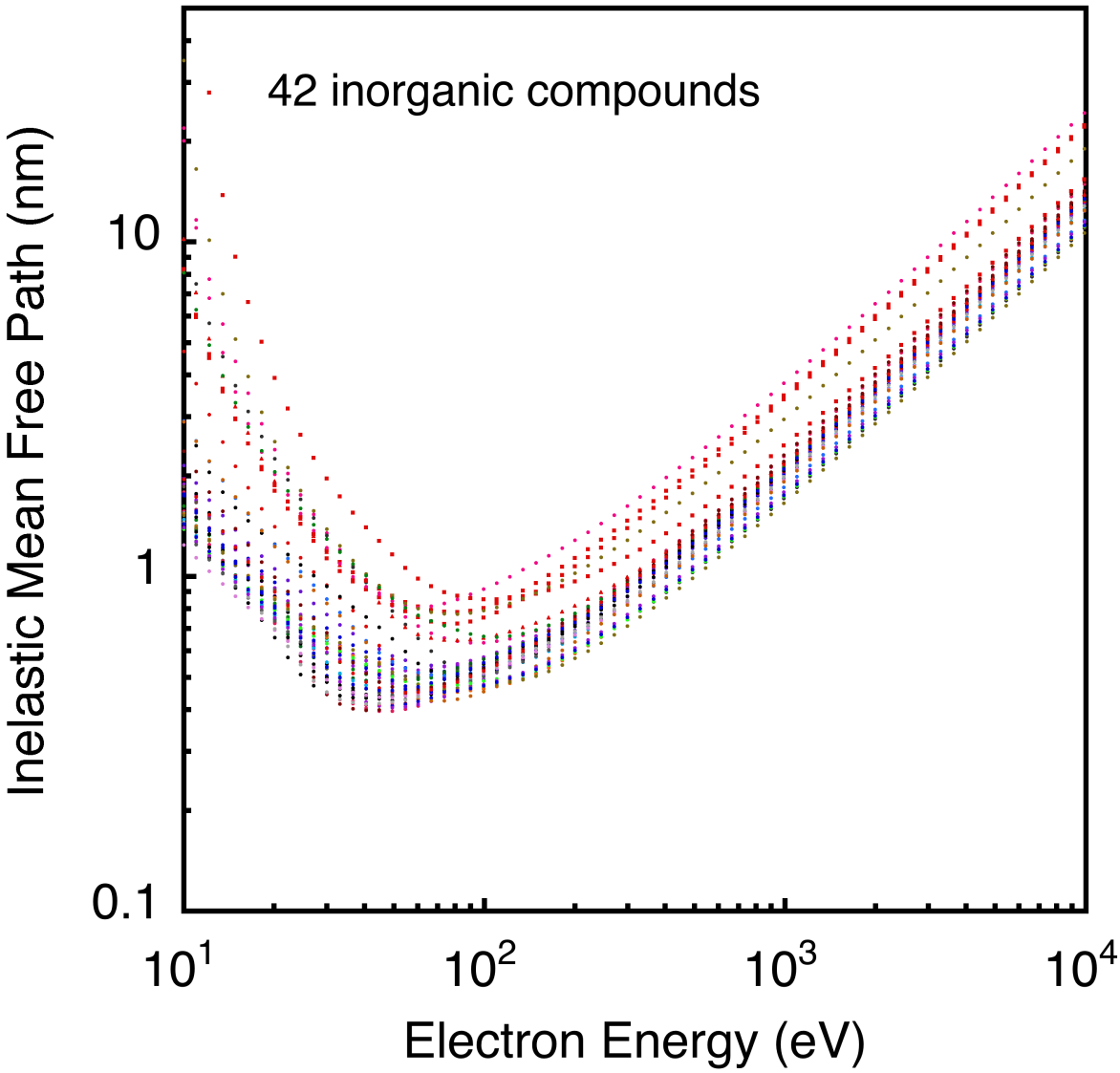
42 inorganic compounds
Inelastic Mean Free Path (nm)
10
1
0.1
10^1
10^2
10^3
10^4
Electron Energy (eV)

Fig. 2.12.2

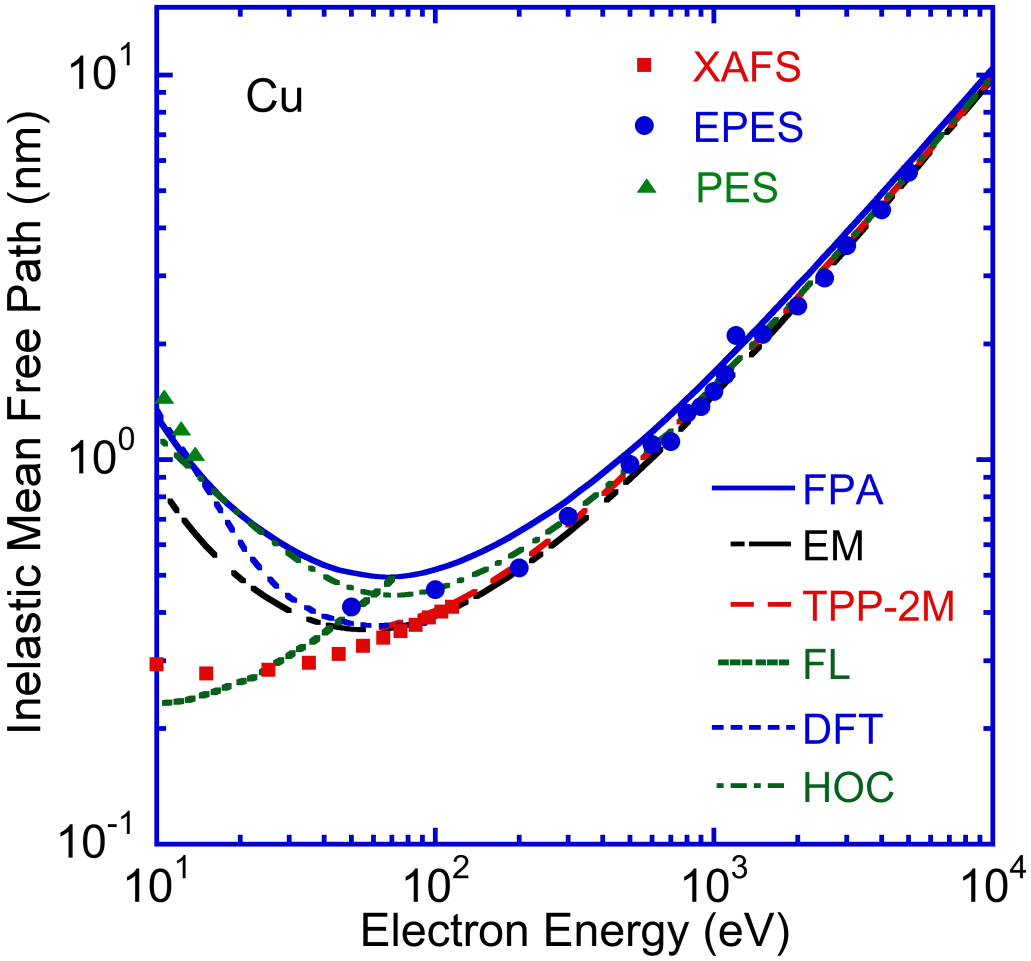
Cu
XAFS
EPES
PES
FPA
EM
TPP-2M
FL
DFT
HOC
Inelastic Mean Free Path (nm)
Electron Energy (eV)
10^1
10^0
10^-1
10^1
10^2
10^3
10^4

Fig. 2.12.3

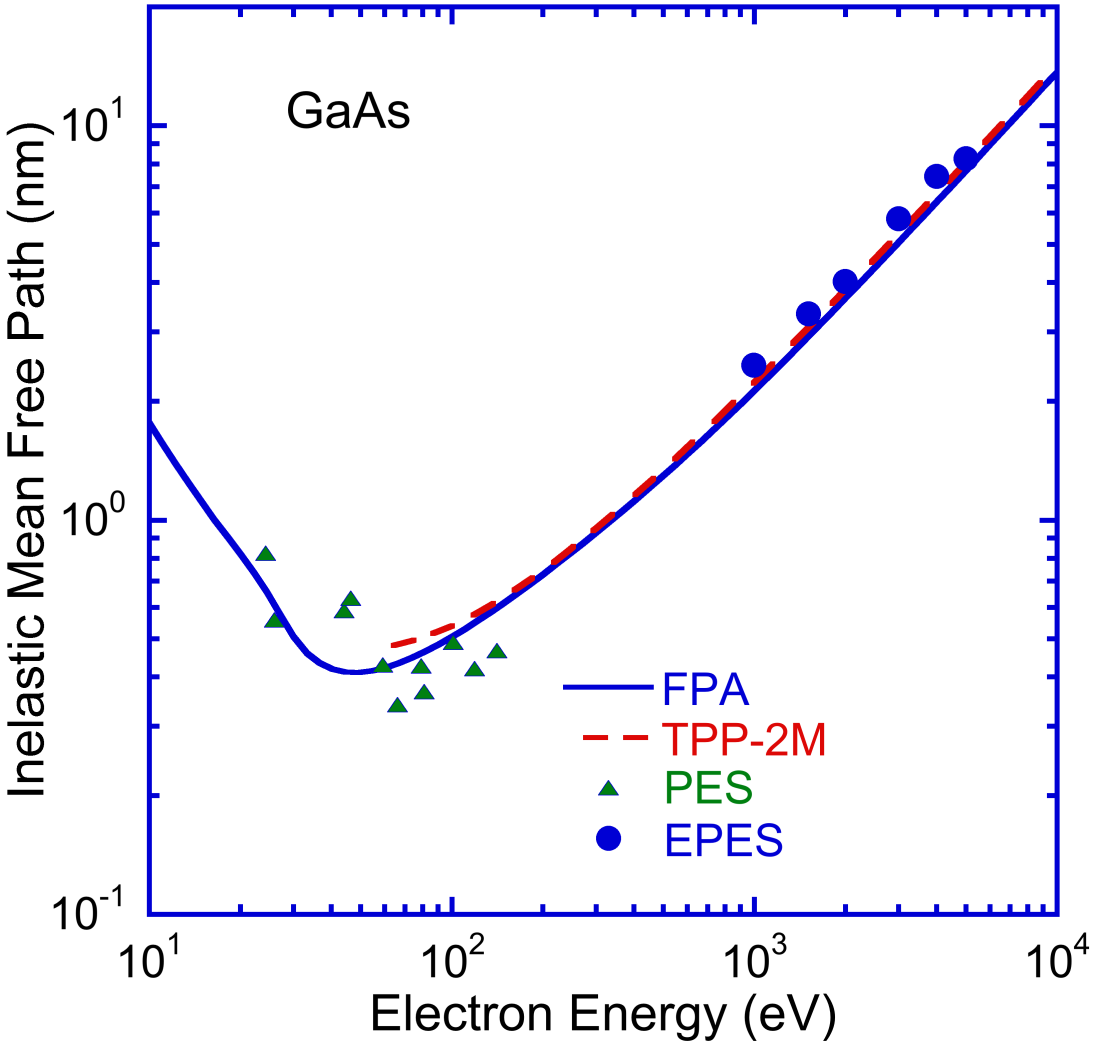
GaAs
Inelastic Mean Free Path (nm)
Electron Energy (eV)
FPA
TPP-2M
PES
EPES

Fig. 2.12.4